

ROF-2 as an Aggregation-Induced Emission (AIE) Probe for Multi-Target Amyloid Detection and Screening of Amyloid Inhibitors

Yijing Tang, Dong Zhang, and Jie Zheng*

Misfolding and aggregation of amyloid peptides into β -structure-rich fibrils represent pivotal pathological features in various neurodegenerative diseases, including Alzheimer's disease (AD), type II diabetes (T2D), and medullary thyroid carcinoma (MTC). The development of effective amyloid detectors and inhibitors for probing and preventing amyloid aggregation is crucial for diagnosing and treating debilitating diseases, yet it poses significant challenges. Here, an aggregation-induced emission (AIE) molecule of ROF2 with multifaceted functionalities as an amyloid probe and a screening tool for amyloid inhibitors using different biophysical, cellular, and worm assays, are reported. As an amyloid probe, ROF2 outperformed ThT, demonstrating its superior sensing capability in monitoring, detecting, and distinguishing amyloid aggregates of different sequences (Amyloid- β , human islet amyloid polypeptide, or human calcitonin) and sizes (monomers, oligomers, or fibrils). More importantly, the utilization of ROF2 as a screening molecule to identify and repurpose cardiovascular drugs as amyloid inhibitors is introduced. These drugs exhibit potent amyloid inhibition properties, effectively preventing amyloid aggregation and reducing amyloid-induced cytotoxicity both in cells and nematode. The findings present a novel strategy to discovery AIE-based amyloid probes and to be used to repurpose amyloid inhibitors, expanding diagnostic and therapeutic options for neurodegenerative diseases while addressing vascular congestion and amyloid aggregation risks.

1. Introduction

The aggregation of amyloid peptides into β -structure-rich fibrils is a well-established pathological hallmark in neurodegenerative diseases (also referred to as protein-misfolding diseases, PMDs), including the aggregation of amyloid- β (A β) in Alzheimer's disease (AD), human islet amyloid polypeptide (hIAPP) in type II diabetes (T2D), human calcitonin (hCT) in medullary thyroid

Y. Tang, D. Zhang, J. Zheng Department of Chemical Biomolecular and Corrosion Engineering The University of Akron Ohio 44325, USA E-mail: zhengj@uakron.edu

The ORCID identification number(s) for the author(s) of this article can be found under https://doi.org/10.1002/smll.202400879

DOI: 10.1002/smll.202400879

carcinoma (MTC), and α -synuclein (α -syn) in Parkinson's disease (PD).[1-3] While clinical cures for neurodegenerative diseases remain elusive, several complex factors contribute to this challenge, including a limited understanding of disease mechanisms, the heterogeneity of pathological features and symptoms, late-stage diagnosis, the absence of reliable biomarkers, and the limited regenerative capacities for the central nervous system.^[4] More importantly, neurodegenerative diseases are often diagnosed at advanced stages when significant damage to the human brain or tissues has already occurred.[5] Early detection is crucial for subsequent effective intervention; however, current diagnostic methods may lack the necessary sensitivity to detect the diseases in their initial stages.

Despite a challenging task, substantial research efforts have been directed toward the development or discovery of either novel amyloid inhibitors to impede the pathological aggregation and misfolding of amyloid peptides or new sensing molecules for the detection of amyloid aggregates. [6–8] From a disease diagnosis viewpoint, fluorophores and dyes, including Thioflavin T (ThT),

Thioflavin S (ThS), 8-anilinonaphthalene-1-sulfonic acid (ANS), and Conge red, [9-11] have been developed for amyloid detection and sensing. These sensing molecules have exploited their fluorescence properties for monitoring the conformational change and aggregation of amyloid proteins, [12-15] quantifying binding sites in amyloid structures, [16-17] detecting and differentiating amyloid aggregates with different structural features,[18,19] staining amyloids aggregates in in vitro, ex vivo, and in vivo, [20-21] and developing amyloid inhibitors and drugs.[22-24] These sensing molecules typically exhibit enhanced fluorescence upon binding to β -sheet-rich fibrils, enabling to monitor and quantify amyloid formation. However, fluorescent molecules commonly used in amyloid detection and sensing exhibit several shared limitations: (i) susceptibility to the aggregation-caused quenching (ACQ) effect, resulting in a decline in fluorescence over time and impacting the reliability of long-term observations;^[25] (ii) the potential for background fluorescence or non-specific binding, leading to false-positive signals and diminished accuracy in distinguishing amyloid aggregates from other cellular proteins;^[26]

16136829, 2024, 36, Downloaded from https://onlinelibrary.wiley.com/doi/10.1002/smll.202400879 by University Of Akron Bierce Library, Wiley Online Library on [06/09/2024]. See the Terms and Conditions (https://onlinelibrary.wiley.com/erms

and-conditions) on Wiley Online Library for rules of use; OA articles are governed by the applicable Creative Commons

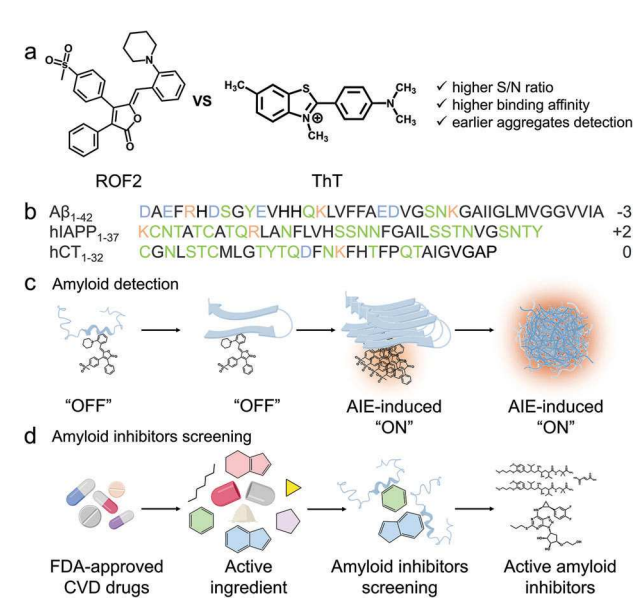


Figure 1. Dual-functional ROF2 fluorescence for amyloid detection and amyloid inhibitor screening. Chemical structure of a) ROF2 and ThT. b) $A\beta$, hIAPP, and hCT sequences, with color codes for positively charged residues (orange letters), negatively charged residues (blue letters), polar residues (green), and non-polar residues (black). c) ROF2 serves as an amyloid probe with an "off-on" switch for the detection of amyloid aggregates. d) ROF2 functions as a screening molecule for amyloid inhibitors, aiming to discover potential amyloid inhibitors.

(iii) a lack of specific targeting mechanisms for various stages of amyloid aggregation, particularly the highly toxic oligomers at the early aggregation stage; ^[27] (iv) possible toxicity, especially at higher concentrations or with prolonged exposure, limiting their (pre)clinical or physiological applications; ^[28] and (v) challenges in penetrating the blood-brain barrier and cellular membranes, as well as poor aqueous solubility. ^[29] These limitations severely hinder their applications for amyloid detection and imaging in in vitro and in vivo cellular environments. ^[11,30–33]

In contrast to those conventional ACQ fluorophores commonly used as amyloid probes, which often experience significant self-quenching, poor photostability, and small Stokes shifts in the aggregated state, aggregation-induced emission (AIE) molecules, as discovered in 2001,^[34] exhibit strong fluorescence in the aggregated state but weak or no fluorescence in the isolated state. The inherent AIE of fluorophores, coupled with the self-aggregation property of amyloid peptides, establishes a synergistic and functionally complementary pairing. This natural paring makes AIE molecules ideal probes for amyloid detection. [35–38] However, beyond the conventional sensing role of AIE molecules, there is a notable lack of scientific exploration into their potential new functions concerning protein aggregates associated with diseases.

In this work, we proposed and demonstrated a new hypothesis, leading to the discovery of an aggregation-induced emission (AIE) molecule of ROF2 with its multifaceted functionalities as an amyloid probe and a screening tool for amyloid inhibitors (**Figure 1**a). ROF2 is a recently developed AIE molecule inspired by its ACQ counterparts of ROF1.^[39] The selection of ROF2 is mainly attributed to its (i) long wavelength emission of

orange-to-red fluorescence, offering the advantage of minimizing tissue auto-fluorescence during detection; (ii) easy sourcing through a one-pot synthesis, enhancing its accessibility and potential for widespread applications; (iii) cell membrane permeability for lipid droplet imaging, suggesting the potential to surpass the blood-brain barrier (BBB) for advanced imaging in neurological studies; and (iv) limited prior exploration, with only one reported research paper available. In contrast to a ThT probe for amyloid detection, which lacks a fluorescence switching on-off mechanism and requires the use of high concentrations, ROF2 not only demonstrated its enhanced sensing capability by emitting fluorescence upon binding to three distinct amyloid peptides — A β , hIAPP, and hCT (Figure 1b,c) but also effectively discriminated between various amyloid aggregates at different aggregation stages, manifesting distinct fluorescence intensities. Further competitive binding tests involving ThT, ROF2, and amyloid peptides showed that ROF2 outperformed ThT in terms of superior sensing performance, characterized by high emission intensity, rapid detection time, and heightened sensitivity, particularly evident in its efficacy against the early stage amyloid species. More importantly, we proposed a novel strategy, suggesting the utilization of ROF2 as a signature molecule for screening effective amyloid inhibitors based on the following hypothesis. In the presence of ROF2, an amyloid inhibitor candidate, and amyloid peptides, the inhibitory efficacy of the amyloid inhibitor candidate on amyloid aggregation is reflected by the absence of direct AIE-induced fluorescence by ROF2, leading to fluorescence quenching. Conversely, unchanged AIE-induced fluorescence indicates a limited or poor inhibitory effect of the amyloid inhibitor candidates on amyloid formation. In line with this hypothesis, employing ROF2 as a screening molecule for experimental screening of potential amyloid inhibitors from 30 FDA-approved cardiovascular (CVD) drugs spanning the years 2006 to 2023 successfully identified several of these drugs as effective amyloid inhibitors (Figure 1d). Specifically, Ali5 demonstrated a strong inhibitory effect on $A\beta$ aggregation, while Tic11, Amb3, and Ang27 exhibited notable inhibitory capabilities on hCT aggregation. However, none of these cardiovascular drugs displayed a significant inhibitory effect on hIAPP aggregation. Ali5 and Tic11 further showcased their inhibitory properties by effectively reducing amyloid-induced cytotoxicity in both neuronal cell models and a worm model. This study introduces a novel strategy, achieving a dual purpose by integrating the development or discovery of amyloid inhibitors through sensing molecules. The rationale for this integration lies in the common foundation shared by both the "inhibition" and "detection" of amyloid aggregates, rooted in molecular interactions between amyloid peptides and specific molecules.[40-41] This approach holds the potential for broader applicability to other fluorescent probes exhibiting high binding affinity to amyloids, making them suitable for use in screening for amyloid inhibitors.

2. Results and Discussion

2.1. AIE Property of ROF2

While the structure of ROF2 has been well characterized by ¹H NMR and ¹³C NMR (Figures S1 and S2, Supporting Information), it remains crucial to validate its aggregation-induced

www.small-journal.com

16136829, 2024, 36, Downloaded from https://onlinelibrary.wiley.com/doi/10.1002/smll.202400879 by University Of Akon Bierce Library, Wiley Online Library on (06/09/2024). See the Terms and Conditions (https://onlinelibrary.wiley.com/rems-ad-conditions) on Wiley Online Library for rules of use; OA articles are governed by the applicable Centarive Commons

emission (AIE) characteristics. As shown in Figure S3 (Supporting Information), we conducted a series of water (poor solvent)/DMSO (good solvent) mixtures by varying the water/DMSO volume ratio from 0/100 to 99/1. This aimed to test the gradual changes in fluorescent emission from a particlefree state to aggregate states. Due to the favorable solubility of ROF2 in DMSO, ROF2 exhibits weak emission upon excitation at 350 nm. However, with the introduction of the poor solvent (water), the mixture becomes increasingly luminescent, accompanied by a noticeable red-shift in the fluorescence emission wavelength. Specifically, upon the addition of water exceeding 60 vol%, ROF2 displayed strong emission, manifesting as vibrant yellow-orange luminescence at 555 nm. Further increasing the water content (>70 vol%) resulted in a reduction in fluorescence intensity, but a significant red-shift from 555 nm (yellow-orange) to 605 nm (orange-red). Quantitatively, ROF2 in 60 vol% and 70-99 vol% water exhibited 15- and 8-12-times higher maximal absorption peaks at 555 and 605 nm than ROF2 in pure DMSO, respectively. This poor solvent-enhanced (i.e., water-enhanced) fluorescence is primarily attributed to the occurrence of aggregation after adding a poor solvent to a good solvent. In the aggregate state, the intramolecular motions of ROF2 become constrained, inhibiting nonradiative transitions and promoting emission. This behavior is a characteristic indicator of the AIE effect, providing conclusive evidence that ROF2 exhibits AIE ac-

For most AIE molecules, the presence of hydrophobic groups is essential to facilitate tight bonding between AIE molecules via hydrophobic interactions. This interaction can further enhance the fluorescence stability of AIE compounds in the aggregate state. However, when designing an AIE probe for detecting amyloid aggregates, it is essential to determine the critical concentration at which ROF2 remains non-fluorescent. This determination helps to avoid undesirable background signals from ROF2 itself and achieve a fluorescence "off-to-on" transition. Therefore, before introducing ROF2 into the amyloid solution, a series of control experiments were conducted by incubating 0.1-10 µм ROF2 with PBS buffer (the identical buffer formulation used in the amyloid aggregation study). The fluorescence spectrum and the UV-irradiated photos in Figure S4 (Supporting Information) clearly show that ROF2 emitted fluorescence in a concentrationdependent manner. Specifically, as the concentrations of ROF2 decreased from 10 to 0.1 µM, the emission intensity of ROF2 gradually decreased from 2342 to 27 a.u. Notably, low concentrations of ROF2 (≤0.2 μm) did not induce any detectable fluorescence emission, as indicated by almost negligible fluorescence signals. To ensure high-to-maximal AIE signals, the higher concentration of ROF2 (i.e., 0.2 µm) was selected as the working concentration to detect amyloid peptides. In another set of controls, 20 µм amyloid peptides (A β , hIAPP, and hCT) were co-incubated with and without 0.2 μM ROF2, aiming to rule out the possibility of ROF-2-induced modulation on amyloid aggregation (Figure S5, Supporting Information). As a result, both pure amyloid systems and ROF-2-amyloid co-incubation systems displayed typical fibrillogenesis kinetics, with comparable saturated fluorescent intensity. In parallel, the AFM images clearly demonstrate the fibrillar structures both before and after the introduction of 0.2 µM ROF2 to the amyloid solutions, affirming that the addition of the probe does not alter the fibril formation process. This comparison supports the effectiveness and non-disruptive nature of $0.2\,\mu M$ ROF2 in detecting amyloid fibrils.

2.2. Light-Up Detection of Amyloid Aggregates by ROF2

To demonstrate the AIE-induced detection ability of ROF2 on amyloid aggregates, we investigated the detection capabilities of 0.2 μM ROF2 when interacting with i) different types of amyloid peptides (i.e., A\beta, hIAPP, and hCT); ii) different aggregation species of amyloid peptides (i.e., monomers, oligomers, and fibrils); and iii) different concentrations of amyloid aggregates (i.e., 0, 20, 40, and 80 µm). As shown in Figure 2a, it is evident that ROF2 exhibited "seed- and concentration-dependent, but sequence-independent" fluorescence emission. Notably, pure ROF2 (gray lines, Figure S6, Supporting Information) itself did not generate any fluorescence signal at 555 nm. This indicates not only the absence of self-aggregation of ROF2 at 0.2 μM, but also ensures that no fluorescence signal from ROF2 contributes to the subsequent signals caused by amyloid aggregation. In contrast, when co-incubating ROF2 (0.2 μ M) with A β , hIAPP, or hCT (20-80 µм) in monomeric, oligomeric, and fibrillar states, all nine AIE-amyloid systems exhibited enhanced emission compared to pure ROF2, albeit to varying extents.

Specifically, ROF2 exhibited remarkably low binding affinities to all three monomeric amyloid systems, resulting in weak emission peaks of 70-159 a.u. at 555 nm. It is worth noting that ROF2- $A\beta$ monomers (80 μM) exhibited a distinct fluorescent peak, primarily due to a faster aggregation rate of $A\beta$ at the lag phase (Figure S5, Supporting Information). In sharp contrast, when introducing ROF2 into a pre-existing amyloid seed solution (i.e., the amyloid oligomer systems), there was a pronounced enhancement in fluorescence intensities across all emission wavelengths from 500 to 700 nm. A substantial increase in the absorption peak with its peak at 555 nm was evident, exhibiting an increase from 171 to 284 a.u. for A β oligomers, from 234 to 440 a.u. for hIAPP oligomers, and from 204 to 355 a.u. for hCT oligomers as the amyloid concentration increased from 20 to 80 µm. Such fluorescence enhancement was further intensified when introducing ROF2 into fibrillar amyloid solutions, as evidenced by a higher peak fluorescence intensity at 555 nm. Quantitatively, the fluorescence intensity of 20–80 μ M A β , hIAPP, or hCT fibrils at 555 nm was 193-340, 297-928, and 170-401 a.u., respectively. These values correspond to 6.7-11.7, 15.6-48.8, and 5.9-16.7 times higher than those observed with ROF2 alone, demonstrating the significant enhancement of fluorescence in the presence of amyloid fibrils. As a comparison, we conducted selectivity studies using BSA, lysosome, and fibrinogen, which are common proteins found in blood plasma, to evaluate the specificity of ROF2. The results, presented in Figure S7 (Supporting Information), show that all three proteins, at concentrations ranging from 20 to 80 µM, exhibited low fluorescence intensities when interacting with 0.2 µm ROF2, and these intensities remained consistent across different concentrations. This indicates that ROF2 does not significantly detect these proteins, thereby demonstrating its selective response to amyloid sequences over these common blood plasma constituents.

Seeing is believing. Upon visual inspection of the inset images in Figure 2a, there are discernible fluorescent variations among

16136829, 2024, 36, Downloaded from https://onlineltbrary.wiley.com/doi/10.1002/smll.202400879 by University Of Akron Bierce Library, Wiley Online Library on [06/09/2024]. See the Terms and Conditions (https://onlineltbrary

onditions) on Wiley Online Library for rules of use; OA articles are governed by the applicable Creative Commons

www.small-journal.com

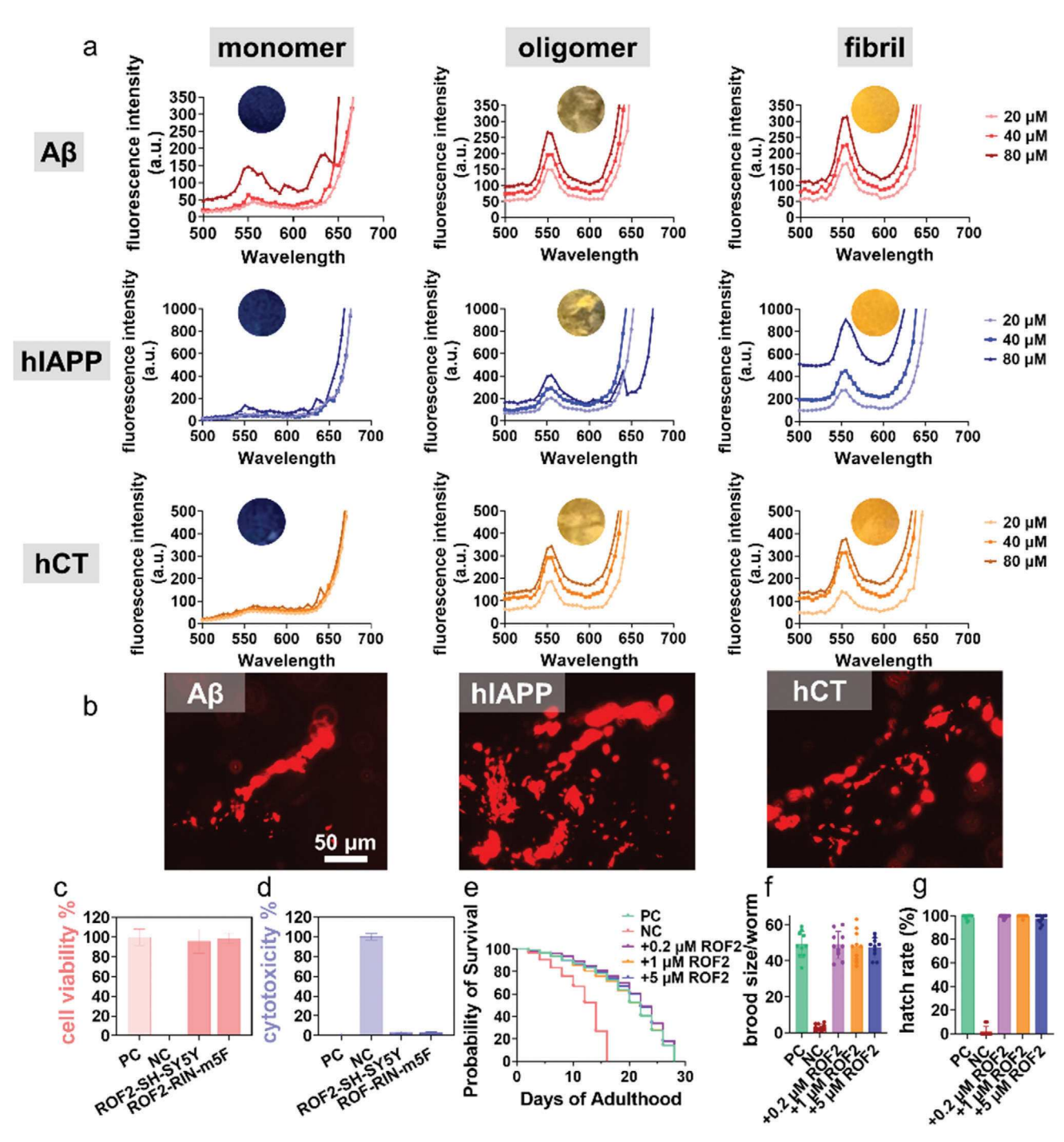


Figure 2. ROF2 exhibits the aggregation- and concentration-dependent emissive property for amyloid detection. a) Fluorescence spectra and optical photos (insets) of ROF2 (0.2 μm) in the presence of monomeric (1st column), oligomeric (2nd column), and fibrillar (3rd column) aggregates of A β (1st row), hIAPP (2nd row), and hCT (3rd row). All the spectra are averaged from triplicate tests and are normalized by subtracting the emission spectra of pure ROF2 to ensure accurate comparisons. b) Representative fluorescence images were obtained from six different locations of amyloid fibrils stained by ROF2. Scale bar is 50 μm. In vitro validation of the non-toxicity of ROF2 using c) MTT for cell viability and d) LDH for cytotoxicity in SH-SY5Y cell model treated with and with 0.2 μm ROF2. In vivo validation of the non-toxicity of ROF2 by e) lifespan probability (n = 120), f) brood size (n = 30), and g) hatching rate (n = 30) in wild-type N2 worms treated with S-complete buffer (PC, green), 0.5 m NaOH (NC, red), 0.2 μm ROF2 (purple), 1 μm ROF2 (orange), and 5 μm ROF2 (blue). Statistical analysis was conducted to compare cells or worms treated with ROF2 to the PC group. No significance was observed between the ROF2-treated group and the PC group.

www.small-journal.com

16136829, 2024, 36, Downloaded from https://onlinelibrary.wiley.com/doi/10.1002/smll.202400879 by University Of Akon Bierce Library, Wiley Online Library on (06/09/2024). See the Terms and Conditions (https://onlinelibrary.wiley.com/rems-ad-conditions) on Wiley Online Library for rules of use; OA articles are governed by the applicable Centarive Commons

different amyloid seeds. Initially, all three kinds of amyloid peptides remained weakly fluorescent when ROF2 was added to the freshly prepared native amyloid solution. However, they became partially emissive with a light yellow glow in the presence of amyloid oligomers and were fully covered in fluorescence with a strong orange light in the presence of amyloid fibrils. Further fluorescence imaging was performed by staining amyloid fibrils with 0.2 µm ROF2, as shown in Figures 2b and S8 (Supporting Information). The comparative images highlight that ROF2 does not detect amyloid monomers, as shown by completely black images. However, the fluorescence significantly increases upon co-incubation with amyloid oligomers and fibrils, visually demonstrating the selective binding and detection ability of ROF2 for amyloid aggregates. This provides a clear contrast to the traditional ThT staining, offering new insights into amyloid oligomer visualization. Collectively, the fluorescence response governed by the ROF2 stacking distance (i.e., aggregation states) endows it with a "seed-dependent and off-on" detection capability, mainly demonstrated in two key features: i) a descending ROF2-amyloid aggregates binding preference of amyloid fibrils > amyloid oligomers > amyloid monomers; ii) a general applicability across various amyloid types, with a descending preference for hIAPP > $A\beta \approx hCT$.

To ascertain the minimum concentration of ROF2 required for detecting different amyloid aggregation states, we tested mature amyloid fibrils at a fixed concentration of 20 µм against varying ROF2 concentrations (from 0.01 to 0.2 µm) and analyzed the fluorescence spectra to calculate the detection limit using the $3\delta/k$ method. As shown in Figure S9 (Supporting Information), ROF2 has particularly low detection limits for A β and hIAPP, showing superior linearity with R values of 0.9810 and 0.9503, respectively. This resulted in detection limits of 0.036 μ m for A β fibrils and 0.058 μM for hIAPP fibrils, highlighting ROF2's exceptional sensitivity toward these amyloid species. However, for hCT fibrils, the fluorescence intensity did not maintain a linear relationship below a concentration of 0.2 μ M (R < 0.95), indicating that concentrations lower than 0.2 µm are less effective for detecting hCT aggregation. This distinction reinforces ROF2's capability in sensitively detecting $A\beta$ and hIAPP fibrils while illustrating its comparative limitation with hCT fibrils at lower concentrations.

As a bio-probe, it is essential to assess its intrinsic toxicity and stability. Given that 0.2 µM ROF2 is sufficiently effective in detecting amyloid aggregates, this concentration was chosen for evaluating its toxicity on in vitro cell models (e.g., human neuroblastoma SH-SY5Y and rat pancreatic insulinoma RIN-m5F) and in vivo nematode model (wild-type N2 worms). As shown in Figure 2c,d, for both SH-SY5Y and RIN-m5F cell lines, 0.2 μм ROF2 showed nearly no cytotoxicity, with 96% and 99% cell viability and 4% and 3% cytotoxicity, respectively. Consistently, $0.2-5~\mu M$ ROF2 showed no discernible impact on the normal activities of worms, including lifespan (Figure 2e), brood size (Figure 2f), and hatch rate (Figure 2g). Specifically, worms treated with 0.5 mm NaOH (used as a negative control, NC, represented in red data) experienced complete mortality after 16 days, exhibited impaired egg-laying capacity (≈2 eggs/worm) and showed a complete absence of hatching (0% hatching success). Conversely, worms treated with S-complete buffer (positive control, PC, green data) demonstrated a normal lifecycle, surviving up to 28 days. These PC worms displayed typical reproductive characteristics,

Small 2024, 20, 2400879

including a standard number of laying eggs per worm (≈49 eggs) and a high hatchability rate (≈99%). For comparison, N2 worms treated with 0.2-5 им ROF2 exhibited a similar trend to the PCtreated worms, as evidenced by i) nearly overlapping lifespan curves, with survival extended up to 28 days; ii) a standard brood size per worm, ranging from ≈47.3 to 48.8 eggs; and iii) a consistently high hatchability rate ranging from 97% to 99%. To further evaluate the serum stability of ROF2 under physiological conditions, we performed an alternative stability test. This involved comparing the fluorescence activity of freshly prepared ROF2amyloid fibril complexes with those incubated in PBS buffer for one week. As demonstrated in Figure S10 (Supporting Information), ROF2 maintained its ability to induce significant fluorescence upon binding to amyloid aggregates even after seven days, effectively confirming its stability under physiological-like conditions. These findings collectively suggest the non-toxic and highstability nature of ROF2, ensuring its safe utilization as an amyloid probe.

2.3. Comparison of ROF2 and ThT as Fluorescent Probes for **Amyloid Detection**

Among fluorescent probes for amyloid detection, thioflavin T (ThT) consistently serves as the gold standard, thus, it was selected as a reference to evaluate the amyloid-probing ability of ROF2. To this end, a series of side-by-side experimental comparisons were conducted, including fluorescence titration (Figures S11-S13, Supporting Information), amyloid fibrillization kinetics (Figure 3d-f), and a competitive test (Figure 3k-m) on $A\beta$, hIAPP, and hCT using both ROF2 and ThT at 0.2 μM as detection probes. Considering the presence of aromatic and hydrophobic structures in ROF2 and amyloid peptides, we initially quantitively analyzed the binding affinity of ROF2 to amyloid fibrils using fluorescence titration. This involved titrating ROF2 (0.2 μм) with increasing amounts of $A\beta$, hIAPP, and hCT, ranging from 0 to 40 μm. During this process, a gradual increase in the peak at 555 nm became evident. As a control, pure ROF2 exhibited a low background, typically ranging from 34 to 66 a.u. according to different batches of experiments. While, upon the addition of ROF2 to 0.625-40 μ M A β (Figure S11a, Supporting Information), hIAPP (Figure S12a, Supporting Information), and hCT (Figure S13a, Supporting Information) solutions, the fluorescence emission at 555 nm increased to 57-266, 77-493, and 46-336 a.u., corresponding to a high S/N ratio of 1.26:5.85, 1.17:7.45, and 1.37:9.95, respectively (Figure 3a-c). In sharp contrast, when 0.2 µM ThT was employed for amyloid detection, only the ThThIAPP systems still exhibited a concentration-dependent fluorescence emission with an increasing S/N ratio from 1.01 to 4.6, as the hIAPP concentration increased from 0.625 to 40 μм. Differently, ThT-A β and ThT-hCT systems completely lost their probing capability, as indicated by the overlapping fluorescence spectrum, with the increasing amyloid concentrations from 0 to 40 µм. Additionally, a more detailed analysis (Table S1, Supporting Information) revealed i) a superior linear fit with all types of amyloid fibrils detected by ROF2, as compared to ThT, as evidenced by a comparable or higher R^2 values of ROF2 = 0.9619 (ThT = 0.7599) for A β fibrils, ROF2 = 0.9141 (ThT = 0.9231) for hIAPP fibrils, and ROF2 = 0.9266 (ThT = 0.3741) for hCT fibrils;

16136829, 2024, 36, Downle

ded from https://onlinelibrary.wiley.com/doi/10.1002/smll.202400879 by University Of Akron Bierce Library, Wiley Online Library on [06/09/2024]. See the Terms

on Wiley Online Library for rules of use; OA articles are governed by the applicable Creative Common

www.small-journal.com

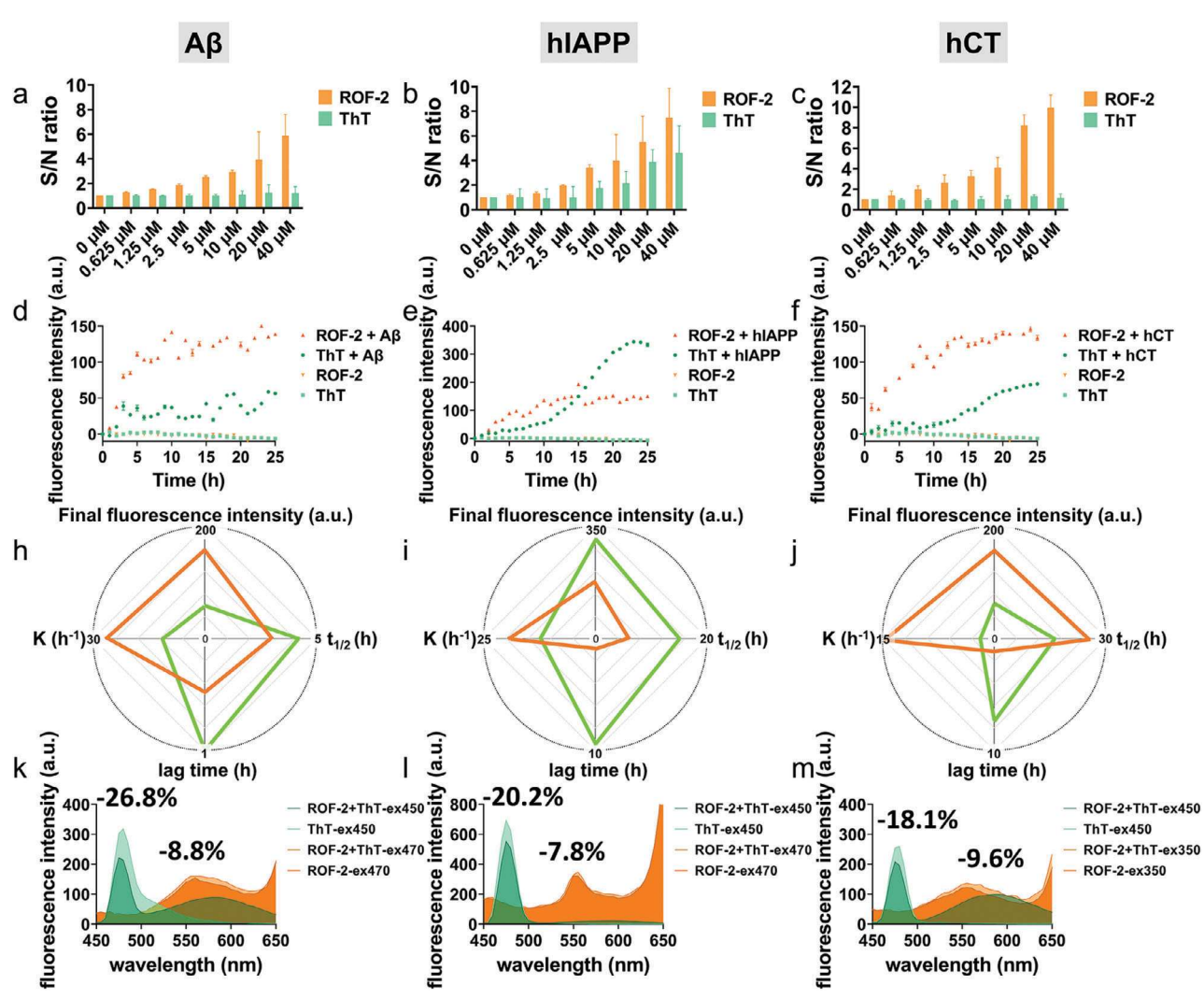


Figure 3. Comparative and competitive binding of amyloid fibrils by ROF2 and ThT. a–c) Signal-to-noise (S/N) ratio comparison of ThT (green) and ROF2 (orange) probes for detecting (a) $A\beta$, (b) hIAPP, and (c) hCT aggregates at concentrations ranging from 0 to 40 μm. Data points were depicted as mean values of repeated measurements (n=3) \pm standard errors of the mean. d–f) Amyloid aggregation kinetics and h–j) Radar charts for evaluating the performance of ThT and ROF2 probes in detecting (d, h) $A\beta$, (e, i) hIAPP, and (f, j) hCT aggregates based on four criteria: final fluorescence increment, aggregation rate (k), aggregation half time (t_{1/2}), and lag-phase time. Data points were depicted as mean values of repeated measurements (n=3) \pm standard errors of the mean. k–m) Competitive binding of ThT and ROF2 to (k) $A\beta$, (l) hIAPP, and (m) hCT fibrils under the same excitation. All the spectra are averaged from triplicate tests.

ii) a lower detection limits with values of ROF2 = $8.95~\mu M$ (ThT = $25.23~\mu M$) for A β fibrils, ROF2 = $13.49~\mu M$ (ThT = $12.97~\mu M$) for hIAPP fibrils, and ROF2 = $12.65~\mu M$ (ThT = $58.13~\mu M$) for hCT fibrils, indicating its statistical effectiveness in amyloid detection; iii) a higher binding affinity, with a lower dissociation constant of ROF2 = $91~\mu M$ (ThT = $638~\mu M$) for A β fibrils, ROF2 = $30~\mu M$ (ThT = $367~\mu M$) for hIAPP fibrils, and ROF2 = $32~\mu M$ (ThT = $452~\mu M$) for hCT fibrils, all together confirming a superior detection performance of the ROF2-amyloid over ThT.

It is widely acknowledged that earlier stages of amyloid species are more toxic than mature amyloid fibrils, making it imperative to design an amyloid probe with the capability to target not only amyloid fibrils but also amyloid oligomers. To examine the earliest amyloid species that can be detectable by ThT and ROF, along with the assessment of their probing capabilities, we then

co-incubated 0.2 μ m ROF2 (orange line in Figure 3d–f) and ThT (green line in Figure 3d–f) with 20 μ m A β , hIAPP, and hCT at 37 °C for 24 h, during which the kinetics of fluorescence intensities were recorded.

As demonstrated in Figure 3d–f, as controls, neither pure ROF2 nor ThT induced any fluorescence enhancement during the incubation period, thus eliminating the possibilities of ROF2 and ThT themselves influencing the amyloid aggregation signal. In parallel, in the presence of amyloid peptides, both ROF2 and ThT were able to capture characteristic sigmoidal nucleation-polymerization curves, but with different kinetics performances. Specifically, in both A β -ROF2/ThT systems (Figure 3d) and hCT-ROF2/ThT systems (Figure 3f), ROF2 exhibited superior probing performance in terms of both emission intensity and the sensitivity toward the earlier amyloid species, as evidenced by i) higher

16136829, 2024, 36, Downloaded from https://onlinelibrary.wiley.com/doi/10.1002/smll.202400879 by University Of Akon Bierce Library, Wiley Online Library on (06/09/2024). See the Terms and Conditions (https://onlinelibrary.wiley.com/rems-ad-conditions) on Wiley Online Library for rules of use; OA articles are governed by the applicable Centarive Commons

saturated fluorescence intensity ($I_{\rm max}=159~{\rm a.u.}$ vs $I_{\rm max}=61~{\rm a.u.}$ for A β and $I_{\text{max}} = 160$ a.u. vs $I_{\text{max}} = 70$ a.u. for hCT); ii) shorter lag phase ($t = 0.5 \text{ h vs } t = 1 \text{ h for A}\beta$ and $t = 0.5 \text{ h vs } t = 7.8 \text{ h for } \beta$ hCT); iii) less time to reach half of I_{max} ($t_{1/2} = 3 \text{ h vs } t_{1/2} = 4.5 \text{ h}$ for A β and $t_{1/2} = 16$ h vs $t_{1/2} = 25$ h for hCT); and iv) faster aggregation rate at $t_{1/2}$ ($k = 27 t^{-1} \text{ vs } k = 13 t^{-1} \text{ for A}\beta \text{ and } k = 15 t^{-1} \text{ vs } k$ = 1.7 t^{-1} for hCT) (Figure 3h,j). In the case of hIAPP-ROF2/ThT systems, it is noteworthy that even a minor ThT concentration (0.2 µm) can still induce a high fluorescence intensity of 330 a.u., surpassing the fluorescent response detected by the same concentration of ROF2 (192 a.u.). While it is interestingly observed that ROF2 triggered the fluorescence signal earlier than ThT, as evidenced by a shorter lag time of 1 h, a reduced half-time of 6 h, and a faster aggregation kinetics of 20 t⁻¹, as compared to 9.5, 16 h, and 13 t⁻¹ for ThT, respectively (Figure 3e,i), confirming a higher sensitivity of ROF2 in detecting earlier hIAPP oligomers.

Considering the "light-on" amyloid-binding capabilities of both ROF2 and ThT as amyloid probes, here we further conducted a new type of competitive test with the aim of determining two crucial aspects: i) whether ROF2 and ThT shared the same binding sites and ii) which of the two amyloid probes exhibits a stronger competitive binding affinity for amyloid species. To this end, two sets of parallel comparisons were performed by incubating amyloid fibrils with (1) ThT at $\lambda_{ex} = 450$ nm (light green) versus both ThT and ROF2 (as the secondary adding probe) at $\lambda_{\rm ex}$ = 450 nm (dark green) and (2) ROF2 at λ_{ex} = 350 nm (light orange) versus both ROF2 and ThT (as the secondary adding probe) at $\lambda_{\rm ex} = 350$ nm (dark orange). Since there is no energy transfer between ThT and ROF2, due to their distinct excitation wavelengths of ThT and ROF2 that do not overlap with each other. Therefore, under the same excitation wavelengths, any reduction in fluorescence intensity upon adding the secondary probe can be attributed to the shared and predated binding sites, in which the extent of reduction reflects the efficiency of binding replacement. The results in Figure 3k-m indicated that both ROF2 and ThT, when used as the secondary probe, induced a reduction in fluorescence intensity, but to different extents. Specifically, the introduction of ROF2 into ThT-binding amyloid fibrils solution (i.e., test 1) caused a more pronounced reduction, as compared to the introduction of ThT into ROF2-binding amyloid fibrils solution (i.e., test 2). These competitive tests clearly indicate the higher binding affinity of ROF2 to amyloid fibrils to effectively displace the pre-existing bounded ThT and impede the displacement by subsequently adding ThT. Quantitively, upon 450 nm excitation, ROF2 effectively competed with ThT for binding sites, resulting in a fluorescence peak reduction of 26.8%, 20.2%, and 18.1% for the A β , hIAPP, and hCT fibril systems, respectively. In contrast, when ThT was introduced into ROF2-bound amyloid fibrils, the binding interaction between amyloid fibrils and ROF2 was less affected under 350 nm excitation, as indicated by a smaller peak reduction of only 8.8%, 7.8%, and 9.6% at 555 nm for A β , hIAPP, and hCT fibril systems, respectively.

2.4. Innovative Application of ROF2 for Screening Amyloid **Inhibitors**

Upon demonstrating the probing capabilities of ROF2, we proposed an intriguing approach to use ROF2 as a signature molecule for screening effective amyloid inhibitors. The underlying hypothesis is that in the presence of ROF2, an amyloid inhibitor candidate, and amyloid peptides, if the amyloid inhibitor candidate can effectively prevent amyloid aggregation, ROF2 will not induce AIE-induced fluorescence directly (i.e., resulting in fluorescence quenching). Conversely, enhanced AIE-induced fluorescence would be observed, indicating a limited or poor inhibitory effect of the amyloid inhibitor candidates on amyloid formation. This working hypothesis, if successful, could have broader applicability to other fluorescent probes for screening amyloid inhibitors.

To test this hypothesis, we first conducted a preliminary test using ROF2 to validate the fluorescence quenching effect as induced by a well-known amyloid inhibitor, (-)-epigallochatechin gallate (EGCG), on amyloid aggregation. As shown in the red lines in Figure 4d,g,j (as controls), the aggregation of pure $A\beta$, hIAPP, and hCT exhibited typical aggregation kinetics with a lag phase of 0.5-15 h, followed by a rapid growth phase of 1-34 h, finally reaching to a saturated phase with the highest ThT intensity of 170, 103, and 718 a.u., respectively. Consistently, when employing ROF2 as an amyloid probe for A β , hIAPP, and hCT fibrils, it also yielded high fluorescence intensities at 465 nm, with values of 285, 330, and 319 a.u., respectively (Figure 4c,f,i). However, when equimolar EGCG was co-incubated with these amyloid peptides, a significant reduction in both ThT and ROF-2 fluorescence intensity was observed. This reduction is quantitively evident by lower ThT and ROF2 fluorescence values of 56 and 218 a.u. for A β , 42 and 191 a.u. for hIAPP, and 70 and 96 a.u. for hCT, corresponding to 87% and 25%, 59% and 42%, and 90% and 70% lower than those of the pure amyloid peptides, respectively (green lines in Figure 4c,d,f,g,i,i). Clearly, the addition of EGCG induced a strong inhibition of amyloid aggregation, resulting in a lower ThT and ROF2 fluorescence, thus confirming the practical utility of ROF2 as a screening tool for amyloid inhibitors.

Next, given the close relationship between AD and CVD and the successful repurposing of CVD drugs as amyloid inhibitors, [22] we proposed to employ ROF2 for experimentally screening potential amyloid inhibitors from CVD drugs approved by the FDA from 2006 to 2023. Prior to amyloid inhibitor screening, since the in vitro preparation of amyloid formation in an aqueous buffer solution, those CVD drugs with low water solubility might encounter challenges in dissolving adequately in water, potentially influencing their binding affinity with amyloids. Twelve of thirty CVD drugs, with water solubility exceeding 20 µm, were selected to access their inhibitory ability against $A\beta$, hIAPP, and hCT aggregation using ROF2 at a molar ratio of drugs/ROF2 = 1:1 (Figure 4a). As shown in Figure 4b,e,h, the saturated fluorescence intensities of pure amyloid aggregation (as positive controls, red bars) were normalized to 100%, while $A\beta$, hIAPP, and hCT with EGCG (as negative controls, green bars) were normalized to 75%, 58%, and 30%, respectively. When comparing the normalized fluorescence differences between the control and the A β -drug systems, only one CVD drug, Ali5, emerged as a potent inhibitor of $A\beta$ aggregation. Evidently, there was a substantial decrease in fluorescence, reaching only 60% of the $A\beta$ intensity, even lower than that of EGCG with 75%, indicating that Ali5 exhibits a stronger inhibitory capacity against A β aggregation than EGCG (Figure 4b,c). Such inhibition was further supported by ThT fluorescence data, in which the co-incubating

16136829, 2024, 36, Downloaded from https://onlinelibrary.wiley.com/doi/10.1002/sml1.202400879 by University Of Akron Bierce Library, Wiley Online Library on [06/09/2024]. See the Terms and Conditions (https://onlinelibrary.wiley.com/term

xonditions) on Wiley Online Library for rules of use; OA articles are governed by the applicable Creative Commons License

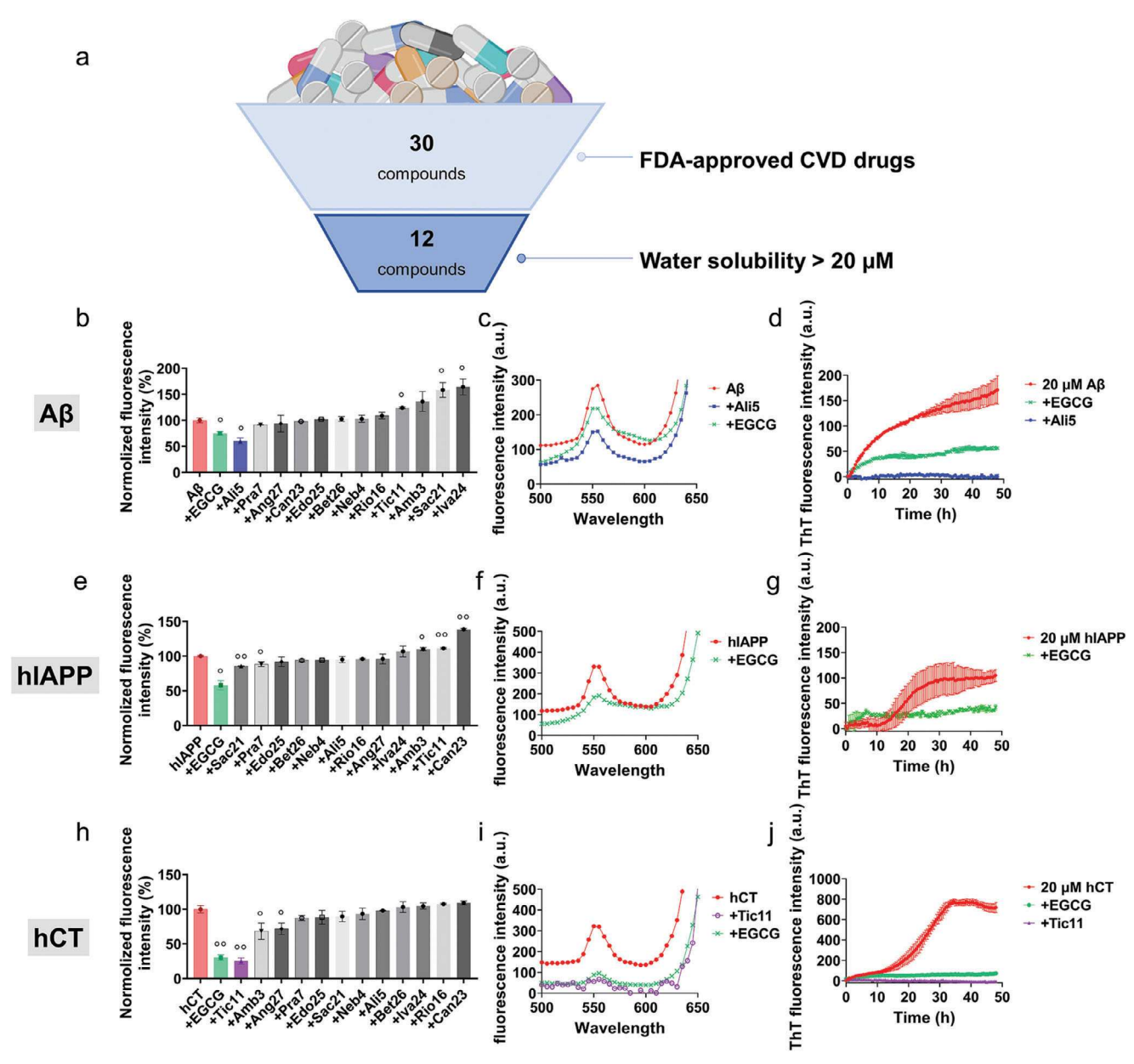


Figure 4. Screening of amyloid inhibitors from FDA-approved CVD drugs Using ROF2. a) Flowchart of screening strategy of CVD drugs as amyloid inhibitors. Twelve CVD drugs were evaluated by ROF2 probes for their effects on b) 20 μm, A β , e) hIAPP, and h) hCT aggregation at an excitation wavelength of 350 nm and emission wavelength of 555 nm. Fluorescence signals were normalized by the fluorescence of pure amyloid peptides being set to 100%. c,f,i) ROF2 fluorescence spectra and d,g,j) ThT aggregative kinetics profiles of 20 μm (c,d) A β , f,g) hIAPP, and i,j) hCT with and without equimolar dose of EGCG (green lines), Ali5 (blue lines), or Tic11 (purple lines). Data points were depicted as mean values of repeated measurements (n = 3) \pm standard errors of the mean. All the spectra are averaged from triplicate tests.

Ali5 with $A\beta$ at an equal molar ratio completely suppressed $A\beta$ aggregation (Figure 4d; Figure S14, Supporting Information).

In the case of hCT systems, three CVD drugs (i.e., Tic11, Amb3, and Ang27) exhibited obvious inhibition capabilities, as evidenced by their relatively weak fluorescence intensities of <80% (Figure 4h). Among these, Tic11 presented a stronger inhibition ability than others, even surpassing EGCG, on hCT aggregation. Quantitively, co-incubating Tic11 with hCT induced a ROF2 fluorescence intensity of 67 a.u. (vs 96 a.u. for EGCG) and a ThT fluorescence intensity of –6 a.u. (vs 70 a.u. for EGCG), cor-

responding to 79% (70% for EGCG) and 100% (90% for EGCG) inhibition (Figure 4i,j; Figure S16, Supporting Information). Unfortunately, none of the CVD drugs showed a significant inhibitory effect on hIAPP aggregation, as indicated by a reduction in ROF2 fluorescence of less than 20% in all the CVD drughIAPP systems (Figure 4e), which was also further corroborated in ThT assays (Figure S15, Supporting Information).

To further validate the inhibition capability of Ali5 on $A\beta$ and Tic11 on hCT, we applied AFM and CD to track amyloid fibril formation and secondary structure changes. As controls, both

16136829, 2024, 36, Downloaded from https://onlinelibrary.wiley.com/doi/10.1002/smll.202400879 by University Of Akron Bierce Library, Wiley Online Library on [0609/2024]. See the Terms and Conditions (https://onlinelibrary.wiley

ditions) on Wiley Online Library for rules of use; OA articles are governed by the applicable Creative Commons

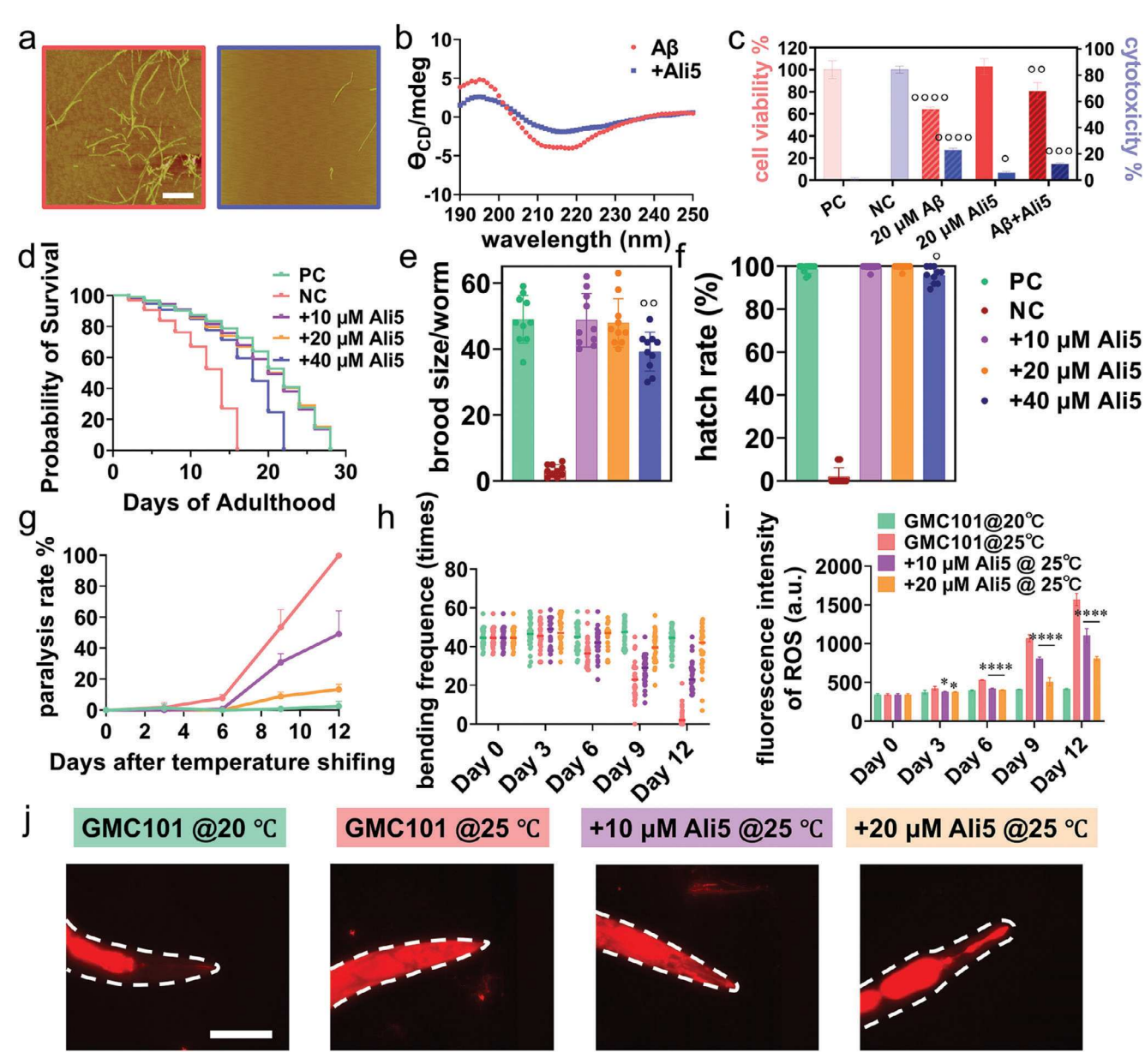


Figure 5. In vitro and in vivo validation of the inhibitory effect of Ali5 on A β aggregation and cytotoxicity. a) AFM images were obtained from six different locations and b) circular dichroism (CD) spectra of pure (a,b) A β (20 μ M) with and without 20 μ M Ali5 after 24 h incubation. c) MTT assay (red bars) for cell viability and LDH assay (blue bars) for cell toxicity when incubating 20 μM Aβ in the presence and absence of equimolar Ali5. Data were normalized by the untreated cell group (positive control, PC, 100% MTT reduction, and 0% LDH activity) and Triton-X-100-treated cells (negative control, NC, 100% LDH activity). Statistical analysis was conducted to compare cells treated with amyloid proteins or ROF2 to the respective control groups ($^{\circ}$, p < 0.05; $^{\circ\circ}$, \tilde{p} , p < 0.001). Data points were depicted as mean values of repeated measurements (n = 3) \pm standard errors of the mean. In vivo validation of Ali5 self-toxicity assessed through (d) lifespan probability (n = 120), e) brood size (n = 30), and f) hatching rate (n = 30) in wild-type N2 worms treated with S-complete buffer (PC, green), 0.5 м NaOH (NC, red), 0.2 μм ROF2 (purple), 1 μм ROF2 (orange), and 5 μм ROF2 (blue). Statistical analysis was conducted to compare cells treated with amyloid proteins or ROF2 to the PC group ($^{\circ}$, p < 0.05; $^{\circ\circ}$, p < 0.01). Paralysis assays for characterizing g) paralysis rate (n = 90), h) bending frequency (n = 90), i) ROS intensity (n = 100), and j) in vivo NIAD-4 staining (n = 30) of age-synchronized GMC101 worms treated with 10 μm (purple) or 20 μm (orange) Ali5 at 25 °C for 12 days. Statistical analysis was conducted to compare cells treated with amyloid proteins or ROF2 to the GMC101@25 °C groups (* , p < 0.05; ** , p < 0.01; *** , p < 0.001). As controls, non-treated GMC101 worms cultured at 20 °C (green) and 25 °C (red) were used as positive and negative controls, respectively.

pure $A\beta$ aggregation (Figure 5a) and hCT aggregation (Figure S17a, Supporting Information) at 20 µм underwent morphological changes and grew into long and dense fibrils with average height/length of 17/1540 nm at 24 h and 20/740 nm at 108 h, respectively. In contrast, the introduction of equimolar Ali5 or Tic11 to a freshly prepared A β or hCT solution (20 μ M) significantly delayed the formation of mature fibrils after 24/108 h incubation, as indicated by the absence of large mature fibrils, but the formation of short fibrils with the average height/length of 10/736 nm for A β -Ali5 system and 6/260 nm for hCT-Tic11

www.small-journal.com

16138582, 2024, 36, Downloaded from https://onlinelibrary.wile;e.cond/doi/10.1002/smll. 202400379 by University Of Akron Bieree Library. Wiley Online Library on [0609/2024]. See the Terms and Conditions (https://onlinelibrary.wiley.com/erms-and-conditions) on Wiley Online Library for rules of use; OA articles are governed by the applicable Creative Commons Licenses

system. From a secondary structure viewpoint, at the beginning of aggregation (0 h), all samples, with and without amyloid inhibitors, displayed a broad negative peak at ≈198 nm, indicating predominant random coil structures for all samples (Figures \$18 and \$19, Supporting Information). As the aggregation proceeded, $A\beta$ alone followed a typical structural transition from the random coil (≈198 nm) to a β-sheet-rich structure (two characteristic peaks at ≈195 and ≈215 nm), finally leading to 39.9% of the random coil and 60.1% of β -sheet after 24 h. In contrast, co-incubating A β with Ali5 delayed their secondary structure transition, as evidenced by less pronounced β -sheet peaks (Figure 5b). Quantitively, the secondary structure distributions calculated from CD spectra revealed that the presence of Ali5 reduced β -sheet structures by 4.5%, but increased α -helix and random coils by 4.3% and 0.2%, clearly reflecting a slower structural transition from random coils to β -structures. Similarly, for hCT, starting from the similar CD spectra with typical random coil structures, the hCT-Tic11 system exhibited a slower conformational transition than pure hCT in three aspects: i) during the 24-h growth stage, pure hCT showed an obvious decline in peak 198 nm, while hCT-Tic11 sample remained almost unchanged for this peak; ii) in the final equilibrium stage of 108 h, hCT displayed deeper peaks at ≈195 and ≈215 nm as compared with hCT-Tic11 system; iii) quantitively, hCT-Tic inhibited the β -sheet formation by 3.6% at the expense of random coil (Figures \$17b and \$19, Supporting Information).

To enhance the clinical relevance of the observed inhibitory performance, we expanded our study by incorporating in vitro cell models and in vivo nematode models to investigate the neuroprotective effects of new-found amyloid inhibitors on amyloidinduced abnormalities (i.e., cell death, worm paralysis, lifespan, brood size, ROS, and bending frequency). As shown in Figures 5c and S17c (Supporting Information), we first applied MTT (red bars, an indication of cell viability) and LDH (blue bars, an indication of cytotoxicity) to i) confirm the toxicity of Ali5 and Tic11 themselves and ii) compare cell systems treated with pure $A\beta/hCT$ to those co-treated with $A\beta$ -Ali5/hCT-Tic11. Here, cells without any treatment were set as positive control (PC), which were normalized as 100% cell viability and 0% cytotoxicity, while cells treated with 10x Lysis buffer were set as negative control (NC), which were normalized as 0% cell viability and 100% cytotoxicity. Based on these controls, pure A β and hCT (20 μ M) led to 64% and 72% cell viability and 27% and 13% cytotoxicity upon 24 h of incubation with cells, respectively, confirming the high toxicity of A β and hCT aggregates to the neuron cells. In sharp contrast, 20 µm pure inhibitors of Ali5 and Tic11 were almost non-toxic to SH-SY5Y cells, as indicated by 103% and 88% of cell viability and 6.7% and 0% of cytotoxicity, respectively. When coincubating corresponding amyloid inhibitor with amyloid peptide (i.e., Ali5 with A β or Tic11 with hCT), both Ali5 and Tic11 exhibited an obvious cytoprotective effect, as evidenced by increased cell viability by 17% and 10% and decreased cytotoxicity by 13% and 15%.

Furthermore, in vivo nematodes were employed as a sophisticated biological model to assess the protective efficacy of Ali5 against A β -induced toxicity, while the hCT nematode model was not available and thus not included. Initially, the wild-type Caenorhabditis elegans (C. elegans) N2 strain, without genetic modifications, was employed to assess the toxicity of Ali5 itself on *C*.

elegans. As detailed in Section 2.2, NC-treated worms (red data in Figure 5d-f) were deceased after 16 days, displaying compromised egg-laying (≈2 eggs/worm) and hatching (0% hatching success) capability. In contrast, PC-treated worms (green data in Figure 5d-f) demonstrated a normal lifecycle with 28 days lifespan, a standard number of eggs laid per worm (\approx 48), and a high hatchability rate (≈99%). For comparison, Ali5-treated N2 worms exhibited a concentration-dependent self-toxicity. Specifically, the survival curve of 10 μm- (purple line) and 20 μm- (orange line) treated N2 worms almost overlapped with the PC group, suggesting minimal or no toxicity of ROF2 at these concentrations. However, a further increase of Ali5 concentration to 40 µM (blue line) resulted in a gradual decline in the survival rate, ultimately reducing their lifespan to 22 days. Consistently, dietary supplementation with 10-20 µM Ali5 maintained a normal brood size of 47.9-48.7 and a hatching rate of 100%, while 40 µм Ali5-treated worms showed a reduction in worm brood size to 39.2 and a worm hatchability of 95%.

Considering the potential false-paralysis signal induced by the self-toxicity of 40 μm Ali5, we opted for 10-20 μm Ali5 to investigate the beneficial effect of Ali5 on AD prevention using transgenic, age-synchronized C. elegans GMC101 strain. Ideally, the GMC101 worm maintains a normal state when cultured at 20 °C. However, it expresses human $A\beta_{1-42}$ in body wall muscle cells, leading to severe age-progressive paralysis upon temperature upshift to 25 °C.[42] GMC101 worms cultured at 20 and 25 °C without any Ali5 supplementation serve as positive control (PC, green data) and negative control (NC, red data), respectively. For the PC group, the untreated GMC101 worms cultured at 20 °C displayed normal activities, as evidenced by i) a low paralysis rate of 2.5%, as compared to 0% at day 0 (Figure 5g); ii) a normal bending frequency of 43 times per min at day 12, as compared to 45 times at day 0 (Figure 5h); and iii) a low reactive oxidative species (ROS) fluorescence enhancement of 73 a.u. after 12 days incubation (Figure 5i). For comparison, the untreated GMC101 worms as the NC group cultured at 25 °C showed a typical time-dependent, progressive paralysis, with a significant difference from PC and NC groups starting from day 6. Specifically, 7.8%, 53.5%, and 100% of the NC groups were identified as paralyzed (i.e., worms with no responsive reaction after touch) on days 6, 9, and 12, respectively. Consistently, the NC groups showed a gradual reduction in bending frequencies from 45 times per min as well as an increase in ROS intensity from 342 a.u. on day 0 to 36 times/530 a.u., 23 times/1070 a.u., 3 times/1570 a.u. on day 6, 9, and 12, respectively.

When feeding 10-20 µm Ali5 to GMC101 worms cultured at 25 °C, Ali5 exhibited a dose-dependent protective effect on reducing A β -induced paralysis symptoms. This was evident through a lower paralysis rate (Figure 5g), faster bending rate (Figure 5h), and lower ROS detection (Figure 5i), as compared with NC groups. Quantitively, all Ali5-treated GMC101 worms remained unparalyzed until day 6, and the paralysis rate of worms treated with 10-20 µm Ali5 was greatly reduced by 23-45% and 51-87% on days 9 and 12, respectively. Similarly, the Ali5-treated GMC101 worms model exhibited comparable or even higher body bend frequencies after 12 days compared to the situation of NC groups after 6 days. Specifically, GMC101 worms treated with 10 µM, and 20 µm Ali5 exhibited 42 and 46 bends on day 6, 28 and 39 on day 9, and 22 and 42 bends on day 12. Moreover, compared to NC

www.advancedsciencenews.com



www.small-journal.com

16136829, 2024, 36, Downloaded from https://onlinelibrary.wiley.com/doi/10.1002/smll.202400879 by University Of Akron Bierce Library, Wiley Online Library on [06/09/2024]. See the Terms and Conditions (https://onlinelibrary.wiley.com/erms

-and-conditions) on Wiley Online Library for rules of use; OA articles are governed by the applicable Creative Commons

groups, GMC101 worms treated with $10-20 \mu M$ Ali5 significantly suppressed the production of ROS by 20-24%, 24-52%, and 30-49% on days 6, 9, and 12, respectively.

Seeing is believing. In line with the abovementioned distinctions between control groups and Ali5-treated groups, the representative worm from PC-, NC-, and 10-20 µm Ali5-treated groups exhibited markedly different mobility behaviors under microscopy (Movie S1, Supporting Information), accompanied by variations in the amount of $A\beta$ accumulation in the head region observed through fluorescence microscopy (Figure 5j). Specifically, PC worms displayed a normal crawl speed and smooth body shape, with no discernible accumulation of A β aggregates in the head region. On the contrary, NC worms exhibited a rigid body, with mobility largely restricted to the head's movement. The fluorescent image clearly showed massive A β deposition in its head region (red fluorescence of 8.0×10^6 a.u.), confirming A β -induced paralysis. In contrast, worms treated with 10 µм Ali5 showed effective recovery from paralysis, demonstrating the ability to move forward with the entire body and a reduction in A β accumulation (red fluorescence of 5.3 × 10⁶ a.u.). Moreover, increasing Ali5 supplementation to 20 μM resulted in worms displaying almost normal activity, with few detectable A β aggregates (red fluorescence of 3.4×10^6 a.u.). Overall, the collective results demonstrate that Ali5 can inhibit A β aggregation and deposition in transgenic AD worms.

3. Conclusion

In this study, we presented and validated a novel design approach for an AIE molecule of ROF2, showcasing its versatile functionalities as an amyloid probe and a screening tool for amyloid inhibitors. As an amyloid fluorescence probe, our design strategy for ROF2 is intended to detect dominant species among monomers, oligomers, and fibrils based on fluorescence intensity. It is optimized for scenarios where one of these species is predominant rather than in well-mixed samples containing equal proportions of monomers, oligomers, and fibrils, a scenario that challenges most existing probes. As compared to gold standard ThT, ROF2 outperformed in various dimensions, including S/N ratio, emission intensity, binding affinity, and sensitivity to early stage amyloid species for demonstrating its efficacy in detecting different amyloid peptides of A β , hIAPP, and hCT at various aggregation stages. Specifically, ROF2 displayed a unique onoff fluorescence response in the presence of amyloid aggregates, offering several advantages. Firstly, ROF2 achieved an ultrahigh signal-to-noise (S/N) ratio by integrating background minimization and precise signal amplification. Secondly, ROF2 proved effectiveness in detecting amyloid oligomers formed during the initial phases of amyloid fibril formation, supported by its high binding affinity to amyloid oligomers. Lastly, ROF2 displayed the ability to differentiate between amyloid monomers, oligomers, and fibrils based on distinct fluorescence intensities. In principle, ROF2's capacity to specifically probe amyloid aggregates is based on its binding to the aggregates, which congregates dispersed ROF2 molecules into close proximity, triggering a significant fluorescence response. This process does not rely on specific molecular interactions with amyloid peptides but rather on the aggregation-induced enhancement of fluorescence when ROF2 molecules are brought together by the amyloid aggregates, particularly through interactions involving the benzene rings within ROF2.

As a screening molecule, ROF2 revealed a novel functionality for screening and identifying amyloid inhibitors from FDAapproved CVD drugs against A β , hIAPP, and hCT aggregation. This screening approach functioned under the working hypothesis that ROF2 would exhibit strong AIE characteristics in the absence of effective amyloid inhibitors, while showing little to no fluorescence or weak fluorescence in the presence of such inhibitors. Through a systematic search, several CVD drugs have been identified and repurposed to effectively inhibit the aggregation of A β and hCT, consequently reducing the cytotoxicity associated with these aggregations in living cells. Specifically, Ali5 displayed a robust inhibitory effect on A β aggregation, while Tic11, Amb3, and Ang27 demonstrated notable inhibitory capabilities against hCT aggregation. However, none of these drugs exhibited inhibitory effects against hIAPP aggregation. More importantly, in a worm model, Ali5 were further shown to be effective inhibitors, protecting transgenic *C. elegans* from Aβ-induced toxicity, as evidenced by improvements in worm paralysis, i.e., lower paralysis rate, ROS, and A β accumulation as well as higher bending frequencies.

In summary, this study not only discovered the AIE molecule ROF2 for its superior and versatile sensing capabilities in monitoring, detecting, and modifying amyloid aggregation as compared to other fluorescent amyloid probes (Figure 6) due to its i) versatile probing capability, targeting multiple types of amyloid aggregates; ii) enhanced binding affinity with amyloid aggregates compared to other materials; and iii) unique ability to differentiate among monomers, oligomers, and fibrils using fluorescence intensity, particularly between oligomers and fibrils, but also introduced an innovative strategy that utilizes ROF2 as a screening tool for repurposing cardiovascular drugs as amyloid inhibitors. The rationale behind this strategy lies in the shared molecular interactions between amyloid peptides and ROF2 molecules, forming the basis for both the "detection" and "screening" of amyloid aggregates by ROF2. In a broader view, considering the potential pathological connection between cardiovascular diseases (CVDs) and neurodegenerative diseases, repurposing CVD drugs as amyloid inhibitors offers a dual benefit by addressing both risk factors associated with vascular congestion and amyloid aggregation, thus achieving a "kill two birds with one stone" strategy in drug discovery for more effective treatment of both cardiovascular diseases and neurodegenerative diseases.

4. Experimental Section

Reagents: Amyloid beta (Aβ $_{1-42}$, ≥ 95%) %), human islet amyloid polypeptide (hIAPP $_{1.37}$, purity ≥ 95.0%), and human calcitonin (hCT $_{1.32}$, purity ≥ 95.0%) were purchased from CPC Scientific (CA, USA). Rofecoxib was purchased from Cayman. 2-(Piperidin-1-yl) benzaldehyde, methanol (≥99.8%), piperidine (99%), 1,1,1,3,3,3-hexafluoro-2-propanol (HFIP,99.9%), 10 mm phosphate-buffered saline (PBS, pH 7.4), dimethyl sulfoxide (DMSO, 99.9%), and thioflavin T (ThT, 98%) were obtained from Sigma–Aldrich (MO, USA). All other chemicals used in this work were of the highest grade.

Synthesis of ROF2: The synthesis of ROF2 was conducted in accordance with a previous study. Piperidine (0.0638 g) was added to a mixture of Rofecoxib (0.2075 g) and 2-piperidinobenzaldehyde (0.51 g) in

16136829, 2024, 36, Downloaded from https://onlinelibrary.wiley.com/doi/10.1002/smll.202400879 by University Of Akon Bierce Library, Wiley Online Library on (06/09/2024). See the Terms and Conditions (https://onlinelibrary.wiley.com/rems-ad-conditions) on Wiley Online Library for rules of use; OA articles are governed by the applicable Centarive Commons

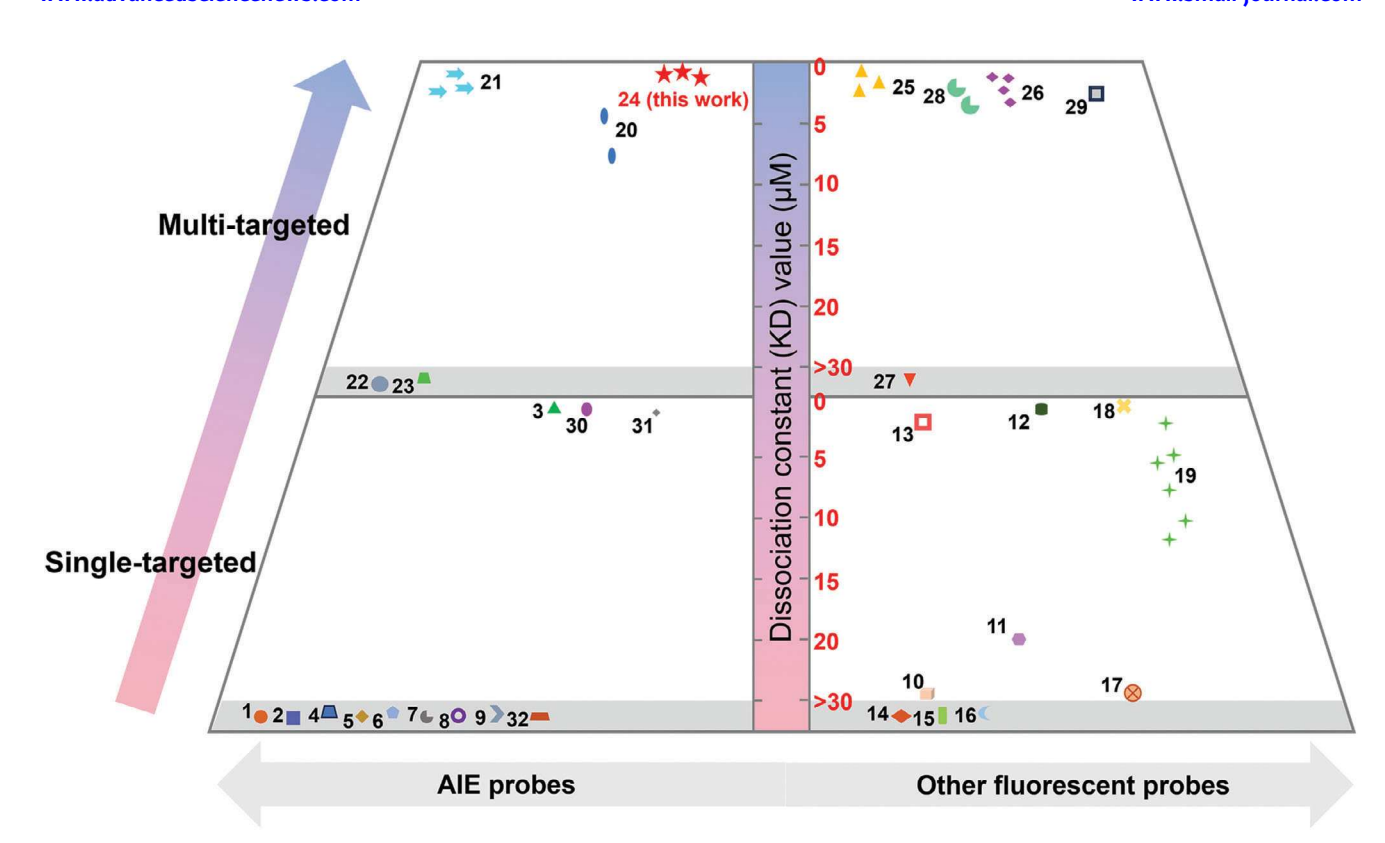


Figure 6. Functional comparison of different amyloid probes in terms of K_D value. References in the gray area indicate that K_D value is not available in the cited literature. All references here are also listed in Table S1 (Supporting Information).

methanol (15 mL). The mixture was stirred at ambient temperature for 12 h in the absence of light. The resulting precipitate was collected by filtration and washed with methanol to ensure the products with high purity. The structure of ROF2 was characterized and confirmed by using ^1H NMR and ^{13}C NMR.

Study of the Aggregation-Induced Emission (AIE) Property of ROF2: To confirm the AIE property of synthetic ROF2, a series of solvent mixtures were prepared using water (a poor solvent) and DMSO (a good solvent) at various volume fractions. Specifically, a total of 2 mL mixtures containing 0/100-99/1 of water/DMSO (v/v%) were prepared for each cuvette. Subsequently, 10 μ L of ROF2 was introduced into each mixture to achieve a final concentration of 10 μ M. The emissions of these solutions were captured under both regular laboratory lighting conditions and 365 nm UV light and then recorded by using the kinetic top-read mode of a Spectra-Max M3 microplate reader (Molecular Devices, CA, USA) with excitation at 350 nm.

To find the critical concentration of ROF2 to induce non-emission (i.e., OFF state), a range of concentrations from 0.1 to $10\,\mu m$ of ROF2 were dissolved in PBS buffer (the same condition for the subsequent experiments), and then captured under both regular laboratory lighting conditions and 365 nm UV light and then recorded by using the kinetic top-read mode of a SpectraMax M3 microplate reader (Molecular Devices, CA, USA) with excitation at 350 nm.

Peptide Purification and Preparation: Upon arrival, all peptides were immediately stored at $-20\,^{\circ}\text{C}$ once arrived. To eliminate any potential preformed amyloid aggregates, the pre-packaged peptides (i.e., $A\beta$, hIAPP, hCT) were re-dissolved in HFIP at the concentration of 1 mg mL $^{-1}$. Subsequently, the HFIP-amyloid solution was incubated at room temperature for 2 h, followed by a 30-min sonication in the ice bath, a 30-min centrifugation at 14 000 rpm and 4 $^{\circ}\text{C}$, and then sub-packaged according to experiment needs. Unless otherwise specified, all peptides underwent a 1-h freeze-drying process to remove HFIP and re-dissolved in different buffers

(containing 5% DMSO or 10% 10 mm NaOH) to reach the desired concentration.

Fluorescence Light-Up Detection of Amyloid Species: Amyloid peptides (20 $\mu\text{M})$ were incubated at 37 °C for 0 h, 20–25 h, and 2 days to obtain monomeric, oligomeric, and fibrillar amyloid species. At different time points, 1 μL ROF2 (0.04 mM) was added to 200 μL amyloid solutions, and the fluorescence wavelengths were recorded by using the kinetic topread mode of a SpectraMax M3 microplate reader (Molecular Devices, CA, USA) between 500 and 700 nm with an excitation wavelength of 350 nm. Subsequently, the wells were then captured under 365 nm UV light.

In order to intuitively visualize the "turn on" fluorescence, the fibrillar amyloid solution was then further observed by using a fluorescence microscope (Echo RVL2-K) under a CY3 filter.

The signal/noise ratio (S/N ratio) was calculated by using the fluorescence intensity with (considered signal intensity) and without (considered noise intensity) amyloid samples at 555 and 480 nm for ROF2 and ThT, respectively.

The apparent binding constant $K_{\rm D}$ of the interaction between ROF2 with amyloid species were quantified by titrating ROF2 (0.2 μ M) with increasing amounts of amyloid peptides (0-40 μ M). Data were analyzed using 1:1 binding model ($\frac{1}{F_t-F_0} = \frac{1}{F_{max}-F_0} + \frac{1}{(F_{max}-F_0)K_D[X]}$, where F_t is the fluorescence intensity during titration, F_0 is the fluorescence intensity before titration, F_{max} is the maximum fluorescence intensity, [X] is the ligand concentration, and K_D is the equilibrium binding constant) and are means (\pm SD) of three binding curves. Each experiment was repeated at least three times, and each sample was tested in triplicate.

Monitoring of Amyloid Aggregation Kinetics Using ROF2 and ThT Probes: Amyloidosis kinetics of amyloid peptides were recorded consistently at 1-h intervals at 37 °C by using a SpectraMax M3 microplate reader (Molecular Devices, CA, USA) and measured at the excitation wavelength of 350 (for ROF2)/450 (for ThT) nm and emission wavelength at 555 and 470–500 nm

under kinetic top-read mode. The ThT and ROF2 stock solution was prepared by dissolving ThT/ROF2 powder in Milli-Q water/DMSO at concentrations of 2 mm and stored in a dark place at room temperature. The stock solutions were then sonicated to a particle-free state and diluted in PBS buffer to 0.04 mm before use. Samples were then prepared on ice by dissolving freeze-dried amyloid peptides in PBS buffer solution (10 mm, pH 7.4), followed by adding 1 µL 0.04 mm ThT/ROF2 to each well.

For the inhibition performance test, samples were prepared by mixing amyloid peptides with and without equimolar amyloid inhibitors and monitored by using 10 μm ThT.

Competition Test Between ROF2 and ThT Probes: The fluorescence wavelengths were then recorded between 500 and 700 nm/450 and 650 nm with an excitation wavelength of 350 nm (ROF2)/450 nm (ThT) by using the kinetic top-read mode of a SpectraMax M3 microplate reader (Molecular Devices, CA, USA). To further compare the binding affinity between ROF2/ThT and amyloid fibrils, the fluorescence intensity spectra were recorded before and after the addition of another 1 μL ThT or ROF2 to the ROF2/ThT-binding amyloid solutions. Each experiment was repeated at least three times, and each sample was tested in triplicate.

Circular Dichroism Spectroscopy (CD): The secondary structures of amyloid aggregation were examined by far-UV CD spectroscopy with a J-1500 spectropolarimeter (Jasco Inc., Japan) using a continuous scanning mode at room temperature. Samples were prepared on ice by dissolving 20 µм freeze-dried hIAPP in PBS buffer (10 mм, pH 7.4) with and without equimolar amyloid inhibitors. To obtain the CD spectrum, 150 µL of samples were pipetted into a 1 mm optical path length CD cuvette, and the spectra of the solution samples were recorded between 190 and 250 nm at 0.5 nm resolution and 50 nm min⁻¹ scan rate. All spectra were analyzed by subtracting the PBS buffer baseline to remove the background signal. The secondary structural contents were determined by using the Beta Structure Selection (BeStSel) algorithm (http://bestsel.elte.hu/).

Atomic Force Microscopy (AFM): The morphology changes of amyloid peptides during aggregation were imaged by using Nanoscope III multimode AFM (Veeco, NY, USA). Samples were obtained from the CD test. To prepare the AFM sample, 10 µL sample solution was deposited on a freshly cleaved mica sheet for 5 min at room temperature, followed by washing three times using Mill-Q water to remove salts and drying with air gas before use. The cantilever resonance frequency was 45-95 kHz. The images (256 pixels \times 256 pixels) were captured using a scan size of 5 μ m. Representative AFM images were obtained by scanning six different locations on the mica surface.

Cell Culture: Human SH-SY5Y neuroblastoma cells (ATCC CRL-2266TM, VA, USA) were used in this study. Cells were cultured in sterile-filtered 1:1 mixture of ATCC-formulated Eagle's Minimum Essential Medium (ATCC, VA, USA) and F12 medium (Sigma-Aldrich, MO, USA) supplemented with 10% fetal bovine serum (FBS) and 1% penicillin/streptomycin. All the cells were maintained in a humidified incubator with 5% CO₂ at 37 °C until cells reached 80% confluence. Cells were then harvested by using 0.25 mg mL⁻¹ Trypsin/EDTA solution (Sigma–Aldrich, MO, USA) and seeded in a 96-well plate (2 \times 10⁴ per well).

MTT and LDH Cytotoxicity Assay: A colorimetric 3-(4,5dimethylthiazole-2-yl)-2,5-diphenyltetrazolium bromide (MTT) metabolic activity assay and lactate dehydrogenase (LDH) assay were used to determine cell viability and cytotoxicity, respectively. Specifically, cells were allowed 24 h to attach the 96-well plate. The medium was then exchanged with amyloid/amyloid inhibitors/amyloid-amyloid inhibitors dissolved in cell medium (2% DMSO) and cultured for another 24 h at 37 °C and 5% CO2 in a humidified incubator. Subsequently, to set up spontaneous/maximum LDH activity, 10 µL of sterile, ultrapure water (as positive control), and 10X Lysis buffer (as negative control) was added to one set of triplicate wells of cells and incubated for 45 min, followed by transferring 50 µL of supernatant medium from each well to a new 96-well plate. Fifty microliters of Reaction Mixture was then added to each sample well, mixed well, and incubated for another 30 min. Finally, 50 μL of stop solution was added to each well, and the absorbance at 490 and 680 nm was measured by using SpectraMax M3 microplate reader. To determine LDH activity, 680 nm absorbance value (background) was subtracted from 490 nm absorbance before the calculation of % cytotoxicity.

Calculate % Cytotoxicity by using the following formula:

% cytotoxicity =
$$\left(\frac{PG - 1 \text{ treated LDH activity} - \text{spontaneous LDH activity}}{maximum LDH activity - \text{spontaneous LDH activity}}\right)$$

$$\times 100\%$$
(1)

For the MTT assay, the old 96-well plate was used. Replaced the residual medium with MTT-medium mixture including 0.5 mg mL⁻¹ MTT and incubated 37 °C for 4 h. After that, replaced the MTT-medium mixture with DMSO to dissolve the formazan crystals (an indicator of the number of live cells). To quantify the cell viability, the absorbance value was read at 540 nm by using a SpectraMax M3 microplate reader, and the cell viability was determined as the percentage of MTT reduction as compared to untreated cells. For both MTT and LDH, each set of samples included 6 wells, and mean \pm SD was reported.

Maintenance of C. elegan Worms: C. elegans strains used in this study i) dvls100[unc-54p::A-beta-1-42::unc543'UTR + mtl-2p::GFP] (GMC101) and ii) wild-type (N2) were provided by the Caenorhabditis Genetics Center (University of Minnesota). To synchronize the population, C. elegans stored at freezing temperatures were thawed at room temperature and then transferred onto a nematode growth medium (NGM) agar plate seeded with Escherichia coli strain (OD50). The organisms were incubated at 20 °C until reaching a gravid state. Subsequently, a bleachsynchronization process was employed to dissolve the worm bodies and retain the eggs. Briefly, gravid adults and eggs were collected, followed by centrifugation. A 5 mL bleach solution (consisting of 2.75 mL Milli-Q water, 1.25 mL 1 M NaOH, and 1 mL bleach) was added to the worm pellet until all the adults were released. Afterward, thorough washing and overnight hatching in an S-complete buffer were carried out. The hatched worms were counted, and their concentration was determined before subsequent use. Once they reached the L4 larval stage, 5-fluoro-2'-deoxyuridine (FudR) was introduced to inhibit the growth of offspring, unless otherwise speci-

Wild-Type N2 C. elegans Lifespan Assay: The lifespan assay was slightly modified from previously described methods.^[43] In brief, agesynchronized worms at the L1 stage were counted and transferred to a 96-well plate, with approximately ten worms per well. At the L4 stage, 30 μL of a 0.6 mm FUDR stock solution was added to each well. Subsequently, 5 µL of the test solution, which included S-complete buffer-DMSO for the positive control, 500 mm NaOH for the negative control, and the tested solutions (i.e., 0.5–5 μM of ROF2 and 10–40 μM of Ali5) for the experimental groups. For each treatment group, a total of 12 wells (≈120 worms) were utilized. The initiation of drug administration was considered as day 0, and the number of surviving worms was recorded under the microscope at two-day intervals until all worms were deceased.

Wild-Type N2 C. elegans Brood Size and Hatching Rate Assay: Agesynchronized worms in the gravid-stage ware randomly assigned to pretreated (i.e., positive control, negative control, 0.5–5 μM of ROF2 and 10– 40 µm of Ali5) NGM plate without FUDR at the concentration of 1 worm per well. After 5 h, all the gravid adults were picked out and the number of hatched eggs was counted for each well. Those eggs were allowed another 1 day to hatch into L1-stage worms. Eggs that did not successfully transition to L1-stage worms were excluded from the hatching rate calculation. Each treatment group utilized a total of 30 wells, corresponding to 30 worms.

Transgenic GMC 101 C. elegans Paralysis Assay: Age-synchronized worms in L4-stage ware randomly assigned to pre-treated (i.e., positive control, negative control, 0.5–5 μm of ROF2 and 10–40 μm of Ali5) NGM plate with FUDR at a concentration of 30 worms per well. They were then incubated at 25 °C to initiate A β . On days 0, 3, 6, 9, and 12, worms were assessed for paralysis, defined as the inability to move during observation and a lack of response to touch-provoked movement with a platinum wire. Representative worms were transferred to a liquid M9 buffer for further photographic documentation. To determine the bending frequency, 1 mL of M9 buffer was added to one of the plates of worms, and the number of bending instances in 30 s was counted.

__smail

16136829, 2024, 36, Downloaded from https://onlinelibrary.wiley.com/doi/10.1002/sml1.202400879 by University Of Akron Bierce Library, Wiley Online Library on [06/09/2024]. See the Terms and Conditions (https://onlinelibrary.wiley.com/erms

and-conditions) on Wiley Online Library for rules of use; OA articles are governed by the applicable Creative Commons

Staining and Microscopy in Transgenic GMC 101 C. elegans: Thirty worms were randomly selected from the day 12 samples of various treatment plates and subjected to incubation with 1 μM NIAD-4 (0.1% DMSO in M9 buffer) for 4 h at room temperature, resulting in robust and reproducible staining. The worm/NIAD solution was subsequently transferred onto 2% agarose pads containing 40 mM NaN3 as an anesthetic on glass microscope slides for imaging. Images were captured using a fluorescence microscope (Olympus IX81) with a $\times 40$ objective and a CY3/DAPI filter. Fluorescence intensity was quantified using ImageJ software and normalized as the corrected total cell fluorescence. Specifically, only the head region was considered due to the high background signal in the guts.

Transgenic GMC 101 C. elegans ROS Assay: Hundred worms were randomly collected from days 0, 3, 6, 9, and 12 in a tube with 500 μL M9 containing 50 μm H2DCF-DA, followed by incubated 2 h in the dark with vortex. Then, worms were washed 2 times with M9 buffer and transferred to a 96-well plate with a concentration of 20 worms per well. SpectraMax M3 microplate reader (Molecular Devices, CA, USA) was used to measure the fluorescence intensity at an excitation wavelength of 485 nm and emission wavelength of 530 nm under top-read mode.

Statistical Analysis: All the data were expressed as means \pm SD of three independent experiments with the statistical analyses conducted on the GraphPad Prism8.0 software (San Diego, USA). The t-test was employed to determine the statistical significance among the groups. $p \le 0.05$ was considered statistically significant.

Supporting Information

Supporting Information is available from the Wiley Online Library or from the author.

Conflict of Interest

The authors declare no conflict of interest.

Data Availability Statement

The data that support the findings of this study are available in the supplementary material of this article.

Keywords

amyloid peptide, biomarker sensor, drug screening, neurodegenerative disease, protein aggregation

Received: February 6, 2024 Revised: April 20, 2024 Published online: May 15, 2024

- M. G. Iadanza, M. P. Jackson, E. W. Hewitt, N. A. Ranson, S. E. Radford, *Nat. Rev. Mol. Cell Biol.* 2018, 19, 755.
- [2] J. Greenwald, R. Riek, Structure 2010, 18, 1244.
- [3] F. Chiti, C. M. Dobson, Annu. Rev. Biochem. 2006, 75, 333.
- [4] W.-Y. Ge, X. Deng, W.-P. Shi, W.-J. Lin, L.-L. Chen, H. Liang, X.-T. Wang, T.-D. Zhang, F.-Z. Zhao, W.-H. Guo, D.-C. Yin, *Biomacromolecules* 2023, 24, 1.
- [5] H. Braak, E. Braak, Acta Neuropathol. 1991, 82, 239.
- [6] Z. Ye, X. Geng, L. Wei, Z. Li, S. Lin, L. Xiao, ACS Nano 2020, 15, 934.
- [7] Y. Ma, Z. Ye, C. Zhang, X. Wang, H.-W. Li, M. S. Wong, H.-B. Luo, L. Xiao, ACS Nano 2020, 14, 11341.

- [8] Z. Ye, L. Wei, Y. Li, L. Xiao, Anal. Chem. 2019, 91, 8582.
- [9] M. Biancalana, S. Koide, Biochimica et Biophysica Acta (BBA)-Proteins Proteomics 2010, 1804, 1405.
- [10] J. Wei, C. Wu, D. Lankin, A. Gulrati, T. Valyi-Nagy, E. Cochran, V. W. Pike, A. Kozikowski, Y. Wang, Curr. Alzheimer Res. 2005, 2, 109.
- [11] A. Aliyan, N. P. Cook, A. A. Martí, Chem. Rev. 2019, 119, 11819.
- [12] M. A. Leissring, A. Lu, M. M. Condron, D. B. Teplow, R. L. Stein, W. Farris, D. J. Selkoe, J. Biol. Chem. 2003, 278, 37314.
- [13] T. Branch, P. Girvan, M. Barahona, L. Ying, *Angew. Chem.* **2015**, *127*, 1243
- [14] A. M. Streets, Y. Sourigues, R. R. Kopito, R. Melki, S. R. Quake, PLoS One 2013, 8, e54541.
- [15] Y. Tang, D. Zhang, Y. Liu, Y. Zhang, Y. Zhou, Y. Chang, B. Zheng, A. Xu, J. Zheng, *Protein Sci.* 2022, 31, 485.
- [16] A. Sidhu, J. Vaneyck, C. Blum, I. Segers-Nolten, V. Subramaniam, Amyloid 2018, 25, 189.
- [17] N. Amdursky, M. H. Rashid, M. M. Stevens, I. Yarovsky, Sci. Rep. 2017, 7, 1.
- [18] A. Alghamdi, S. Forbes, D. J. Birch, V. Vyshemirsky, O. J. Rolinski, Arch. Biochem. Biophys. 2021, 704, 108886.
- [19] Y. Tang, D. Zhang, Y. Zhang, Y. Liu, Y. Miller, K. Gong, J. Zheng, Commun. Biol. 2022, 5, 1.
- [20] Y. Zhang, Y. Tang, Y. Liu, D. Zhang, J. Zheng, Adv. Funct. Mater. 2021, 31, 2102978.
- [21] M. T. Elghetany, A. Saleem, Stain Technol. 1988, 63, 201.
- [22] Y. Tang, Y. Liu, Y. Zhang, D. Zhang, X. Gong, J. Zheng, ACS Chem. Neurosci. 2021, 12, 1419.
- [23] Y. Tang, D. Zhang, Y. Zhang, Y. Liu, X. Gong, Y. Chang, B. Ren, J. Zheng, ACS Appl. Bio Mater. 2020, 3, 8286.
- [24] Y. Tang, D. Zhang, X. Gong, J. Zheng, Chem. Sci. 2022, 13, 7143.
- [25] W. Z. Yuan, P. Lu, S. Chen, J. W. Lam, Z. Wang, Y. Liu, H. S. Kwok, Y. Ma, B. Z. Tang, Adv. Mater. 2010, 22, 2159.
- [26] R. A. de la Faverie, A. Guédin, A. Bedrat, L. A. Yatsunyk, J. L. Mergnyet, Nucleic Acids Res. 2014, 42, e65.
- [27] Y. Tang, D. Zhang, X. Gong, J. Zheng, Adv. Funct. Mater. 2022, 32, 2208022
- [28] Y. Tang, D. Zhang, X. Gong, J. Zheng, Sensors Diagnostics 2023, 2, 1469.
- [29] Z.-Y. Zhang, Z.-J. Li, Y.-H. Tang, L. Xu, D.-T. Zhang, T.-Y. Qin, Y.-L. Wang, Biosensors 2023, 13, 990.
- [30] M.-M. Xu, W.-M. Ren, X.-C. Tang, Y.-H. Hu, H.-Y. Zhang, Acta Pharmacol. Sin. 2016, 37, 719.
- [31] C. Bertoncini, M. Soledad Celej, Curr. Protein Pept. Sci. 2011, 12, 206.
- [32] W. Fu, C. Yan, Z. Guo, J. Zhang, H. Zhang, H. Tian, W.-H. Zhu, J. Am. Chem. Soc. 2019, 141, 3171.
- [33] J. Qi, X. Hu, X. Dong, Y. Lu, H. Lu, W. Zhao, W. Wu, Adv. Drug Delivery Rev. 2019, 143, 206.
- [34] J. Luo, Z. Xie, J. W. Lam, L. Cheng, H. Chen, C. Qiu, H. S. Kwok, X. Zhan, Y. Liu, D. Zhu, Chem. Commun. 2001, 18, 1740.
- [35] H. Arora, M. Ramesh, K. Rajasekhar, T. Govindaraju, Bull. Chem. Soc. Jpn. 2020, 93, 507.
- [36] Y. Zhang, C. Ding, C. Li, X. Wang, Adv. Clin. Chem. 2021, 103, 135.
- [37] F. Gao, J. Chen, Y. Zhou, L. Cheng, M. Hu, X. Wang, RSC Medicinal Chem. 2023, 14, 2231.
- [38] Y. Tang, D. Zhang, Y. Zhang, Y. Liu, L. Cai, E. Plaster, J. Zheng, J. Mater. Chem. B 2022, 10, 2280.
- [39] X. Wang, W. Liu, X. Lin, L. Chen, Z. Wang, Z. Xie, L. Wang, M. Hu, H. Jiang, L. Xie, *Dyes Pigm.* 2022, 198, 109992.
- [40] M. Groenning, J. Chem. Biol. 2010, 3, 1.
- [41] A. Lorenzo, B. A. Yankner, Proc. Natl. Acad. Sci. USA 1994, 91, 12243.
- [42] N. V. Kalmankar, H. Hari, R. Sowdhamini, R. Venkatesan, J. Med. Chem. 2021, 64, 7422.
- [43] G. M. Solis, M. Petrascheck, JoVE 2011, 49, e2496.